APPLIED RESEARCH

Fluid-structure interaction analysis of transcatheter aortic valve implantation

Ivan Fumagalli*[1] | Rebecca Polidori‡[2] | Francesca Renzi‡[2] | Laura Fusini[3,4] | Alfio Quarteroni[1,5] | Gianluca Pontone[3] | Christian Vergara[2]

[1]MOX, Dipartimento di Matematica, Politecnico di Milano, Milan, Italy
[2]LaBS, Dipartimento di Chimica, Materiali e Ingegneria Chimica, Politecnico di Milano, Milan, Italy
[3]Department of Perioperative Cardiology and Cardiovascular Imaging, Centro Cardiologico Monzino IRCSS, Milan, Italy
[4]Department of Electronics, Information and Biomedical Engineering, Politecnico di Milano, Milan, Italy
[5]Institute of Mathematics, École Polytechnique Fédérale de Lausanne, Lausanne, Switzerland, *Professor Emeritus*

Correspondence
*Ivan Fumagalli, MOX, Dipartimento di Matematica, Politecnico di Milano, piazza Leonardo da Vinci 32, 20133 Milan, Italy.
Email: ivan.fumagalli@polimi.it

‡Rebecca Polidori and Francesca Renzi contributed equally to this work.

Present Address
R. Polidori: Dipartimento di Biotecnologie mediche e Medicina traslazionale, Università degli Studi di Milano, Milan, Italy.
F. Renzi: Dipartimento di Scienze Chirurgiche Odontostomatologiche e Materno-Infantili, Università di Verona, Verona, Italy.

Summary

Transcatheter aortic valve implantation (TAVI) is a minimally invasive intervention for the treatment of severe aortic valve stenosis. The main cause of failure is the structural deterioration of the implanted prosthetic leaflets, possibly inducing a valvular re-stenosis 5-10 years after the implantation. Based solely on pre-implantation data, the aim of this work is to identify fluid-dynamics and structural indices that may predict the possible valvular deterioration, in order to assist the clinicians in the decision-making phase and in the intervention design. Patient-specific, pre-implantation geometries of the aortic root, the ascending aorta, and the native valvular calcifications were reconstructed from computed tomography images. The stent of the prosthesis was modeled as a hollow cylinder and virtually implanted in the reconstructed domain. The fluid-structure interaction between the blood flow, the stent, and the residual native tissue surrounding the prosthesis was simulated by a computational solver with suitable boundary conditions. Hemodynamical and structural indicators were analyzed for five different patients that underwent TAVI – three with prosthetic valve degeneration and two without degeneration – and the comparison of the results showed a correlation between the leaflets' structural degeneration and the wall shear stress distribution on the proximal aortic wall. This investigation represents a first step towards computational predictive analysis of TAVI degeneration, based on pre-implantation data and without requiring additional peri-operative or follow-up information. Indeed, being able to identify patients more likely to experience degeneration after TAVI may help to schedule a patient-specific timing of follow-up.

KEYWORDS:
Transcatheter aortic valve implantation , fluid-structure interaction , image-based simulations , computed tomography , patient-specific analysis , in silico predictive investigation

1 | INTRODUCTION

Aortic Stenosis (AS) is the most frequent pathology involving cardiac valves, and it is a typical consequence of aging, due to valvular cusps calcification[1]. It affects about 50% of subjects over 85 years old in the western world, with a classification as

severe AS in 4% of the cases and a 2-year mortality rate of 80% for untreated patients[2,3,4,5]. The treatment for this pathology is the replacement of the aortic valve, either by open-heart Surgical Aortic Valve Replacement (SAVR) or by Transcatheter Aortic Valve Implantation (TAVI). The latter is a minimally invasive technique consisting in the deployment of a stented prosthesis inside the native aortic valve, by means of a percutaneous catheter, possibly associated with a balloon expansion to restore the patency of the aortic orifice. This procedure, introduced in 2002, was initially designed for patients with high surgical risk, but it has recently been extended to low-risk patients: in 2019, TAVI procedures in the United States exceeded the number of SAVR by more than 25%[5], and the PARTNER 3 clinical trial[6] showed how TAVI entails a shortened hospitalization time, strongly reduced post-intervention risks, and improved quality of life.

The currently expected durability of TAVI is about 5-10 years[7], after which different complications may arise: an irregular or eccentric native annulus may yield paravalvular leak, stent migration, hemolysis or an asymmetric deformation of the prosthetic leaflets[8]; the balloon expansion may damage the vascular wall[9]; Structural Valve Deterioration (SVD), namely the degeneration of the prosthetic leaflets tissue, can induce transvalvular regurgitation or stenosis[10]. The latter, provoked by the irreversible development of pannus, fibrosis, and calcification, yields a thickening, delamination, and possibly perforation of the leaflets, resulting in the main cause of TAVI failure[11,12].

Since many of the aforementioned complications manifest only years after the implantation, anticipating their onset would help to set up preventive measures to avoid or reduce their negative effects. Recent clinical studies have investigated the onset of SVD: a 5-year follow-up analysis has identified some possible patient-related factors such as gender, body surface area, and native annulus diameter[10], and other studies conjectured that the cause is to be looked for in alterations in the flow-induced stress on the prosthesis[13,12]. However, nowadays the long-term assessment of TAVI has two strong limits: first, it is a relatively new technology, therefore little follow-up data is available after 10-15 years; second, the available data regards older generation devices implanted on elderly patients, usually presenting additional comorbidities and having a limited life expectancy[14].

In this respect, computational analysis can help providing insight on TAVI function and limitations, as well as allow the study of actual and potential scenarios, in order to support the clinician's decisions in the pre-intervention design phase and in the post-intervention timing of follow-up. The computational study of TAVI has undergone a very strong increase in recent years[15]. Structural analysis by the Finite Element Method (FEM) has been mainly employed to simulate the implantation and assess the stress induced on the native valve and aortic root, the generation of gaps between the stent and the wall, and stress-induced electrophysiological abnormalities[16,17,18]. Computational Fluid Dynamics (CFD) investigations have provided a detailed description of the blood flow, and it has mainly focused on the evaluation of paravalvular regurgitation, Wall Shear Stress (WSS) and the associated thrombogenicity and SVD, and turbulent characteristics[19,20,21]. Combining the two approaches, Fluid-Structure Interaction (FSI) analyses can complete and improve the accuracy of the results mentioned above, in particular in terms of the stress exchanged between the blood flow, the prosthesis, and the surrounding native structure. FSI works on TAVI have been carried out both in the case of realistic[22,7] and patient-specific geometries[8,23], however, no correlation of computational results with SVD, with the aim of assessing the role of hemodynamics in the deterioration of TAVI, is currently available in the literature.

The main objective of this paper is to propose predictive hemodynamic indices able to provide indications about the degeneration in patients undergoing TAVI. Our approach is to avoid the direct modeling of valve dynamics and degeneration process, rather to identify quantities that correlate with SVD, albeit not directly causing it. To this aim, we carry out FSI simulations able to account for the interaction between blood, stent graft, leaflets and aortic annulus. Our goal is to describe hemodynamics and structural behaviour in the early post-implantation scenario, virtually designed starting from the pre-operative case. The setup of the computational model is based only on data available before the implantation, with no need for peri-operative or follow-up data, and it encompasses the segmentation of the patient-specific aortic root and ascending aorta, a geometric virtual implantation of the prosthesis' stent – including the cluttering effect of calcifications on the native leaflets – and an analysis of hemodynamical quantities and the stresses exchanged among the prosthesis and the native tissue. The classification of the results is then compared with the information on the different patients' 5-10 years follow-up outcome in terms of valve degeneration.

The paper is organized as follows. In Section 2, we describe the segmentation and virtual implantation procedure for the geometry reconstruction and the generation of the computational mesh (Section 2.2), as well as the numerical model (Section 2.3). In Sections 3 and 4 we present the results of the application of the reconstruction procedure on five patients and of the corresponding FSI simulations, respectively, and we discuss their significance as indicators for SVD.

2 | MODELS AND METHODS

In this section, we present the medical images at disposal, the image-processing procedure for the reconstruction of the patient-specific geometries, and the mathematical and numerical model for the description of the aortic blood flow and its interaction with the prosthesis stent and the tissue surrounding the prosthesis. These represent the building blocks of our computational investigation, which encompasses the following steps:

1. reconstruction of the patient-specific pre-implantation geometry (see Section 2.2 – Step 1), based on CT data (Section 2.1);
2. virtual implantation of the valve prosthesis (Section 2.2 – Steps 2-3);
3. simulation of the fluid-structure interaction in the resulting virtual post-intervention settings (Section 2);
4. analysis of the results and comparison among the patients at disposal (Sections 3 and 4);
5. identification of predictive indices to discriminate the degenerate cases, based only on pre-operative data (ibidem).

One of the main assumptions of the present work consists in the belief that the physical processes determining SVD are more likely associated with the high flow velocity and the high shear stress sustained by the valve leaflets during the systolic phase[19,24]. Although this assumption should be supplemented by observations on the diastolic flow and on the high pressure gradients exerted on closed leaflets, in this first work we aim at understanding if the systole alone could provide useful predictive indications about the degenerative cases. Moreover, by addressing just the systolic phase, we can assume that the prosthetic leaflets adhere to the stent: this assumption simplifies the reconstruction of the patient-specific geometry (cf. Section 2.2 - Step 3).

We also assume that most of the mechanisms leading to prosthesis degeneration are due to the interaction between the blood and the prosthesis. Under this assumption, the aortic wall can be considered as being rigid (cf. Section 2.3).

Our study is based on data concerning only pre-operative conditions, with the aim of providing clinical indications about the TAVI implantation before the procedure, during the decision-making process.

2.1 | Patients data

Preoperative CT images of five patients that underwent TAVI were collected at Centro Cardiologico Monzino in Milano, Italy. The identification of patients has been made anonymous for the publication of the present work. The data were acquired at late diastole, with a spacing of 0.4 mm in the three directions. Three of the patients under investigation experienced SVD, while the other two did not: in the what follows, we will thus refer to the former patients as DEG patients, and to the latter ones as NODEG patients. A balloon-expandable Edwards SAPIEN XT valve (Edwards Lifesciences) was implanted in all the analyzed subjects: it consists of a trileaflet valve made of bovine pericardium mounted on a balloon-expandable cobalt-chromium stent with an external diameter of 23 mm and a height of 14.5 mm. On the ventricular side of the stent frame, an inner polyethylene terephthalate fabric skirt is applied[25,26].

2.2 | Domain reconstruction from clinical imaging data

For each patient, we reconstructed her/his specific geometry of the aortic root, ascending aorta and calcium deposits starting from the CT images described in Section 2.1. In such geometries, we proceeded with a virtual implantation of the Biological Heart Valve (BHV). The entire procedure, outlined in Fig. 1, was carried out using the Vascular Modeling Toolkit (vmtk, http://www.vmtk.org[27]) and the ParaView (https://www.paraview.org) visualization software, and its steps are described in what follows.

Step 1: Reconstruction of the aortic lumen and the calcifications

The aortic lumen was reconstructed by means of a level-set segmentation based on a marching cubes algorithm[28], with a colliding-front initialization as proposed in[29] for vascular structures. The positions of the coronary ostia were identified, but the coronary arteries were not segmented, as we assume a negligible outgoing flow through them during systole. On the segmented aortic wall, we determined the intersection between the leaflets and the aortic wall by manually tracing via VMTK, over the

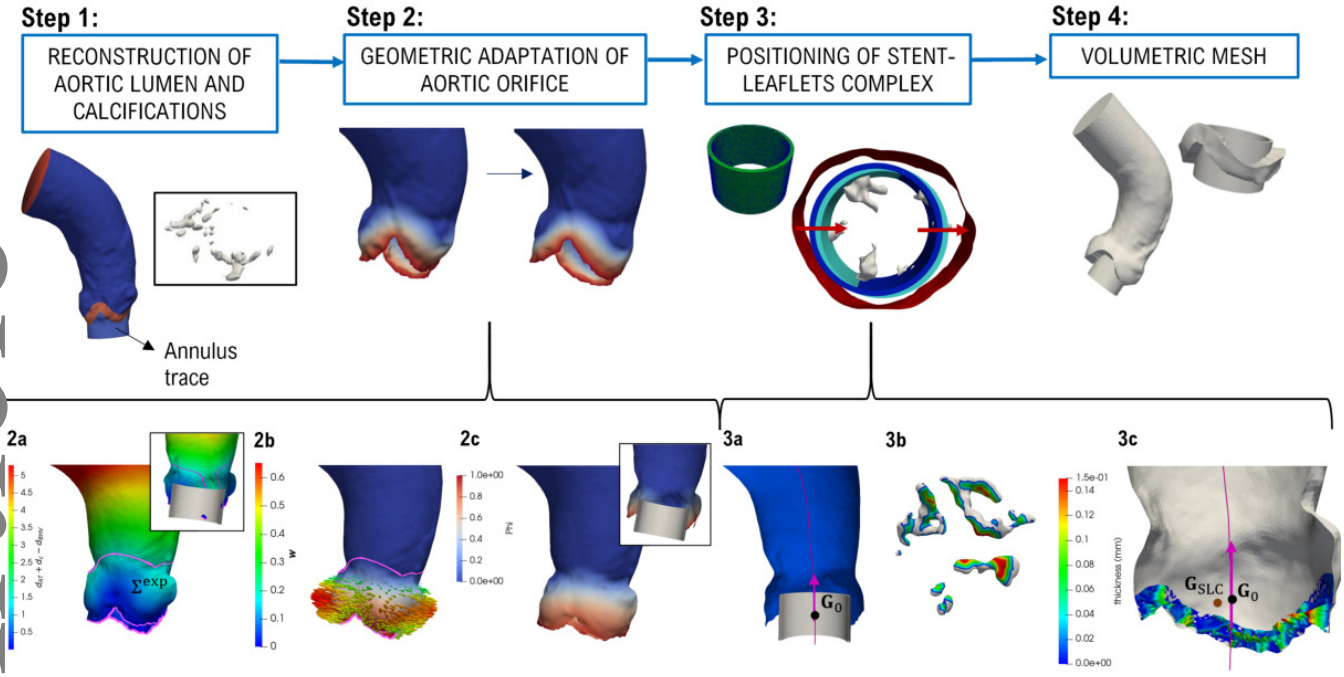

FIGURE 1 Overall reconstruction procedure and sub-procedures for Steps 2 and 3. *Step 1*: segmentation of the aortic lumen and the calcification deposits from CT images; *Step 2*: virtual expansion of the aortic orifice to account for an oversized BHV; *Step 3*: virtual implantation of the BHV in the aortic orifice; *Step 4*: generation of the volumetric mesh for the fluid and the solid computational domains. Zoom on Step 2: *2a*: distance field $d_{AT} + d_c - r_{BHV}$ for the definition of Σ^{exp} (inside the pink border, see point 1. of Section 2.2 - Step 2) to expand because the segmented native annulus is too narrow to fit the BHV (see box at top right); *2b*: scalar field φ (point 2. of Section 2.2 - Step 2) and resulting warping vector field $\mathbf{w}$ (in arrows, point 3. of Section 2.2 - Step 2); *2c*: warped aortic root, in which the BHV fits (box at top right). Zoom on Step 3: *3a*: clip of the domain (blue) with the BHV (gray) centered in $\mathbf{G}_0$ and aligned along the centerline direction $\mathbf{e}_c$ (pink arrow) – see point 1. of Section 2.2 - Step 3; *3b*: segmented calcifications, colored by their thickness (point 2. of Section 2.2 - Step 3); *3c*: extruded annulus trace $\widetilde{\Sigma}_{AT}$ (colored by calcification thickness) and position of the new barycenter $\mathbf{G}_{SLC}$ (points 3-5. of Section 2.2 - Step 3);

imaging data, the ventricle-facing border of such intersection. Then, we isolated a ring shaped region extending for 3 mm from such intersection: in the following, this region will be denoted as *annulus trace* (see Fig. 1 - Step 1).

From the same CT images, we also reconstructed the calcium deposits populating the aortic root, since their distribution affects the positioning of the prosthetic valve during its implantation. The calcifications were segmented by thresholding the gray level of the CT images at 900 HU (see Fig. 1 - Step 1).

Step 2: Geometric adaptation of the aortic orifice

In many cases, the BHV is oversized with respect to the patient's orifice diameter (see box in Fig. 1 - 2a), and the implantation procedure encompasses a balloon expansion of the patient's annulus. To simulate such expansion, we devised the following procedure to locally deform the aortic wall Σ^{wall}:

1. definition of the region $\Sigma^{exp} \subset \Sigma^{wall}$ to expand as a function of the distance of each point of the domain with respect to the upstream border of the annulus trace (see Fig. 1 - 2a):

$$\Sigma^{exp} = \{\mathbf{x} \in \Sigma^{wall} : d_{AT}(\mathbf{x}) + d_c(\mathbf{x}) - r_{BHV} < tol_{exp}\}, \quad (1)$$

where d_{AT} is the distance from the annulus trace, d_c the distance from the vessel centerline, r_{BHV} the radius of the prosthesis ($r_{BHV} = 11.5$ mm for the SAPIEN XT valve under investigation), and tol_{exp} is a patient-specific parameter calibrated considering the particular shape of the aortic root;

2. definition of a smooth scalar field $\varphi : \Sigma^{\text{exp}} \to [0,1]$ ranging from 0 to 1 running from the downstream to the upstream border of Σ^{exp}, as the solution of a Laplace-Beltrami problem[30,31] (see Fig. 1 - 2b);

3. computation of the warping amplitude

$$w(\mathbf{x}) = t_{\text{leaf}} + t_{\text{stent}} - \alpha(d_{\text{c}}(\mathbf{x}) - r_{\text{BHV}}), \tag{2}$$

where $t_{\text{leaf}} = 3$ mm is the thickness of the stenotic leaflets as from[32], including calcifications, t_{stent} is the thickness of the stent wall ($t_{\text{stent}} = 1$ mm for the SAPIEN XT valve under investigation), and α is a scaling parameter to be chosen. This original definition of the warping amplitude is made of two contributions. The term $t_{\text{leaf}} + t_{\text{stent}}$ expands the lumen according to the thickness of the stent and of the native leaflets pressed against the wall. The term $d_{\text{c}}(\mathbf{x}) - r_{\text{BHV}}$, instead, accounts for the circularizing effect of the balloon expansion. In particular, for each point $\mathbf{x} \in \Sigma^{\text{exp}}$, we consider the difference between its distance from the centerline and the nominal stent radius r_{BHV}, and we locally expand or contract the lumen depending on the sign of such difference;

4. deformation of the fluid domain according to the vector field

$$\mathbf{w}(\mathbf{x}) = w(\mathbf{x}) \frac{1 - \cos\left(\pi(2\varphi(\mathbf{x}) - \varphi(\mathbf{x})^2)\right)}{2} \mathbf{n}_{\text{rad}}, \tag{3}$$

displayed in Fig. 1 - 2b, where $\mathbf{n}_{\text{rad}} = \mathbf{n} - (\mathbf{n} \cdot \mathbf{e}_{\text{c}})\mathbf{e}_{\text{c}}$ is the radial component – i.e. orthogonal to the lumen centerline direction $\mathbf{e}_{\text{c}}$ – of the vector $\mathbf{n}$ normal to Σ^{wall}. The enlarged aortic root $\widetilde{\Sigma}^{\text{exp}} = \{\mathbf{x} + \mathbf{w}(\mathbf{x}) : \mathbf{x} \in \Sigma^{\text{exp}}\}$, obtained by warping by $\mathbf{w}$ the segmented one Σ^{exp}, is now wide enough for the BHV to fit (see Fig. 1 - 2c).

The scaling parameter α affects the shape of the deformed wall: for $\alpha = 1$, the resulting aortic root would be perfectly cylindrical as the BHV stent; for $\alpha = 0$, the shape of the aortic root, albeit enlarged, would be preserved as the native one. To account for an intermediate configuration, we chose the value $\alpha = \frac{1}{2}$ for all the patients under investigation.

Step 3: Virtual implantation of the Biological Heart Valve model

In the hypothesis that the prosthetic valve leaflets completely adhere to the stent during the systolic phase, we modeled the prosthesis as a hollow cylinder with the nominal size and thickness of the stent, representing both the actual stent and the open leaflets. This is compatible with our aim to find easily computable hemodynamic indices that show a correlation with SVD, without directly investigating the development of the degeneration process. From now on, we denote this structure as the *Stent-Leaflets Complex* (SLC). This choice avoids the complex reconstruction of the prosthetic leaflets geometry and the modeling of its dynamics, thus reducing the overall computational time needed for both the reconstruction procedure and the subsequent FSI simulation.

Under these assumptions, the virtual insertion of the SLC consisted in the following steps (see Fig. 1 - Step 3):

1. positioning of the SLC at the barycenter $\mathbf{G}_0$ of the aortic orifice, aligned along the lumen centerline direction $\mathbf{e}_{\text{c}}$ (see Fig. 1 - 3a);

2. computation of the calcium deposits thickness along each radial direction (Fig. 1 - 3b);

3. extrusion of the annulus trace towards the inner side of the lumen, according to the calcium thickness: the deformed trace is denoted by $\widetilde{\Sigma}_{\text{AT}}$ and displayed in Fig. 1 - 3c;

4. computation of the average radial distance $\mathbf{d} = \frac{1}{|\widetilde{\Sigma}_{\text{AT}}|} \int_{\Sigma_{\text{AT}}} \left[(\mathbf{x} - \mathbf{G}_0) - \left((\mathbf{x} - \mathbf{G}_0) \cdot \mathbf{e}_{\text{c}}\right) \mathbf{e}_{\text{c}}\right]$ of $\widetilde{\Sigma}_{\text{AT}}$ from $\mathbf{G}_0$, in the plane orthogonal to the centerline direction $\mathbf{e}_{\text{c}}$;

5. translation of the SLC according to the radial distance computed at point 4: its new position will be in $\mathbf{G}_{\text{SLC}} = \mathbf{G}_0 + \mathbf{d}$, as shown in Fig. 1 - 3c.

Step 4: Generation of the volumetric meshes

Once the virtual implantation of the SLC is completed, we project the annulus trace onto the SLC outer surface. The three-dimensional region comprised between the trace and its projection is defined as the *Landing Zone* (LZ) of the prosthesis into the vessel. This region summarizes in a single mechanical component the valve annulus, the native leaflets, and the calcium deposits (see Fig. 2 - Landing Zone).

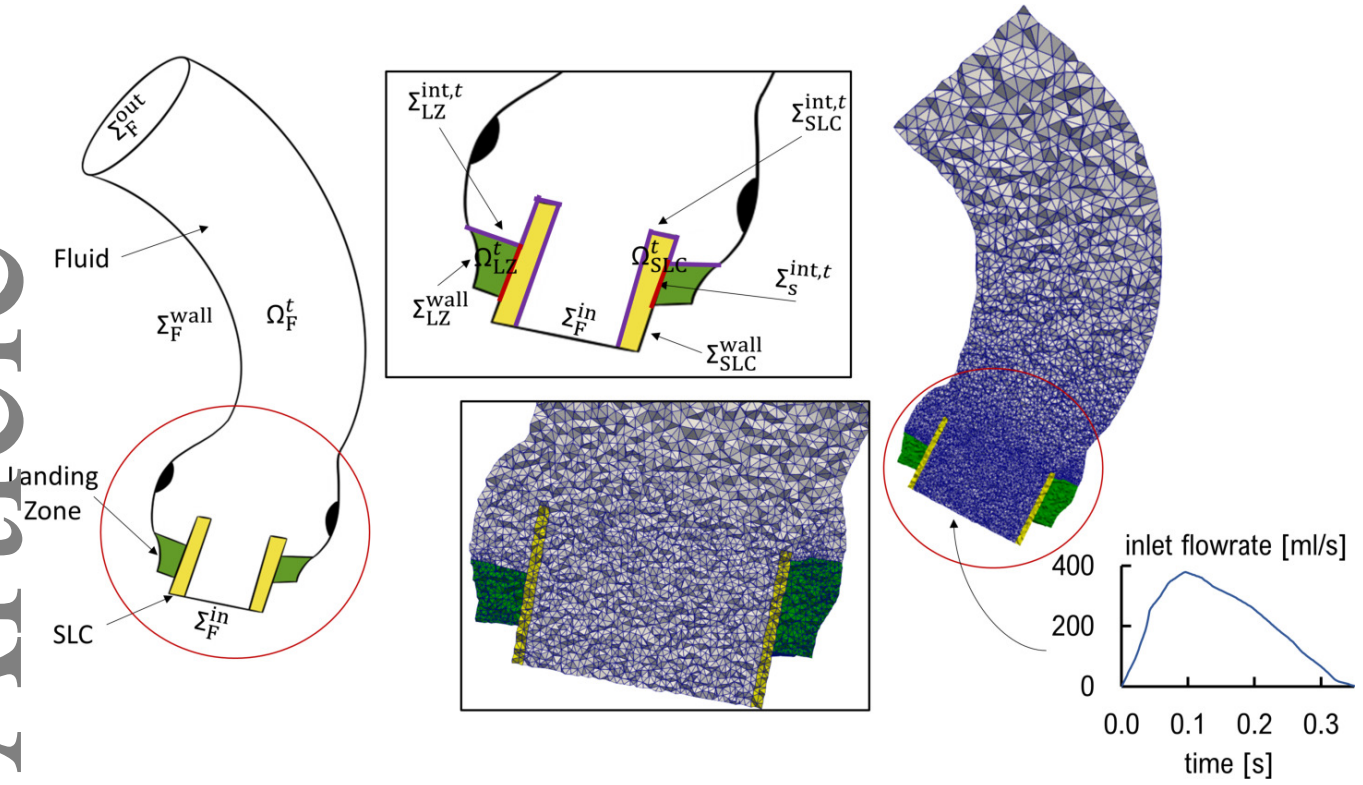

FIGURE 2 Model of the computational domain and volumetric mesh of the patient DEG2: in blue the fluid domain, in green the landing zone and in yellow the SLC, in purple the fluid-structure interface, in red the interface between SLC and LZ. Bottom right: physiological flowrate profile from [33], imposed as inlet boundary conditon.

Combining all of the previously reconstructed surfaces and volumes, we obtain the computational domain depicted in Fig. 2, left: the SLC in yellow is in contact with the LZ in green and with the fluid domain Ω_F^t. In all the previous steps, partial surface remeshing is used to guarantee that the interfaces are conforming. The fluid domain is topologically a tube, and the two structures are hollowed cylindrical volumes, thus a tetrahedral volumetric mesh is generated for each of them, after a local mesh refinement in the aortic root as shown in Fig. 2. The SLC and LZ are combined into a single mesh by juxtaposition.

2.3 | Numerical model

The computational domain of interest is made of a fluid component $\Omega_F^t \subset \mathbb{R}^3$, consisting in the aortic root and the ascending aorta, and a structural component $\Omega_S^t = \Omega_{SLC}^t \cup \Omega_{LZ}^t \subset \mathbb{R}^3$, consisting in the LZ and the SLC, as depicted in Fig. 2. We model blood as an incompressible homogeneous Newtonian fluid, as commonly accepted for large vessels, thus its flow dynamics is described by the Navier-Stokes equations in the Arbitrary Lagrangian-Eulerian (ALE) formulation [34,35], to account for the displacement of the SLC and LZ. The aortic wall is treated as rigid, whereas the dynamics of the moving structures is modeled by the equations of linear elasticity in the fixed reference domain $\widehat{\Omega}_S$, in Lagrangian formulation. We indicate by $\widehat{\cdot}$ the quantities in the reference domain, while a superscript t denotes the moving domain and boundaries: e.g., the current configuration of the fluid domain at time t is $\Omega_F^t = \mathcal{L}_t(\widehat{\Omega}_F)$, where $\mathcal{L}_t$ is the ALE map. The fluid and the structure interact through the interface $\widehat{\Sigma} = \widehat{\Sigma}_{SLC}^{int} \cup \widehat{\Sigma}_{LZ}^{int} \subset \partial\widehat{\Omega}_S$, corresponding to $\Sigma^t \subset \partial\Omega_F^t$ in the moving frame of the fluid and indicated in purple in Fig. 2. The rest of the structure boundary is consider rigid, in accordance with the choice made on the aortic wall. We also define the internal interface $\widehat{\Sigma}_S^{int}$, between the SLC Ω_{SLC} and the landing zone Ω_{LZ}, indicated in red in Fig. 2.

The strong formulation of the coupled problem reads as follows:

Given the initial blood velocity $\mathbf{u}_0 = \mathbf{0}$, for each time $t > 0$, determine $\mathbf{u}$, the blood pressure p, the displacement $\widehat{\mathbf{d}}$ of the structure, and the fluid mesh displacement $\widehat{\mathbf{d}}_F$, such that:

$$
\begin{cases}
\rho_f \left(\frac{\partial \mathbf{u}}{\partial t} + ((\mathbf{u} - \mathbf{u}_{\text{ALE}}) \cdot \nabla)\mathbf{u} \right) - \operatorname{div} \mathbf{T}_{\text{F}}(\mathbf{u}, p) = \mathbf{0} & \text{in } \Omega_{\text{F}}^t, \\
\operatorname{div} \mathbf{u} = 0 & \text{in } \Omega_{\text{F}}^t, \\
\mathbf{u} = \mathbf{u}_{\text{in}} & \text{on } \Sigma_{\text{F}}^{\text{in}}, \\
\mathbf{T}_{\text{F}}(\mathbf{u}, p)\mathbf{n} = p_{\text{out}}\mathbf{n} & \text{on } \Sigma_{\text{F}}^{\text{out}}, \\
\mathbf{u} = \mathbf{0} & \text{on } \Sigma_{\text{F}}^{\text{wall}}, \\
\mathbf{u} = \frac{d\mathbf{d}}{dt} & \text{on } \Sigma^t, \\
\mathbf{T}_{\text{S}}(\mathbf{d})\mathbf{n} = \mathbf{T}_{\text{F}}(\mathbf{u}, p)\mathbf{n} & \text{on } \Sigma^t, \\
\rho_{\text{S}} \frac{\partial^2 \widehat{\mathbf{d}}}{\partial t^2} - \operatorname{div} \widehat{\mathbf{T}}_{\text{S}}(\widehat{\mathbf{d}}) = 0 & \text{in } \widehat{\Omega}_{\text{S}}, \\
\widehat{\mathbf{d}} = \mathbf{0} & \text{on } \partial\widehat{\Omega}_{\text{S}} \setminus \widehat{\Sigma}, \\
-\Delta \widehat{\mathbf{d}}_{\text{F}} = \mathbf{0} & \text{in } \widehat{\Omega}_{\text{F}}, \\
\widehat{\mathbf{d}}_{\text{F}} = \widehat{\mathbf{d}} & \text{on } \widehat{\Sigma}, \\
\widehat{\mathbf{d}}_{\text{F}} = \mathbf{0} & \text{on } \partial\widehat{\Omega}_{\text{F}} \setminus \widehat{\Sigma},
\end{cases}
\tag{4}
$$

where $\mathbf{u}_{\text{ALE}} = \frac{\partial \widehat{\mathbf{d}}_{\text{F}}}{\partial t} \circ \mathcal{L}_t$ is the velocity of the fluid domain, $\mathcal{L}_t$ being defined as $\mathcal{L}_t(\widehat{\mathbf{x}}) = \widehat{\mathbf{x}} + \widehat{\mathbf{d}}_{\text{F}}(\widehat{\mathbf{x}})$, ρ_{F} and ρ_{S} are the densities of the fluid and the structure components, and $\mathbf{u}_{\text{in}}$ and p_{out} are prescribed boundary data (see Section 2.4). The fluid Cauchy stress tensor $\mathbf{T}_{\text{F}}(\mathbf{u}, p)$ is defined as

$$\mathbf{T}_{\text{F}}(\mathbf{u}, p) = -p\mathbf{I} + \mu_{\text{F}}(\nabla \mathbf{u} + \nabla \mathbf{u}^T),$$

where μ_{F} is the dynamic viscosity of blood. The Piola-Kirchhoff stress tensor $\widehat{\mathbf{T}}_{\text{S}}$ of the linear elastic structure is

$$\widehat{\mathbf{T}}_{\text{S}}(\widehat{\mathbf{d}}) = \lambda_{\text{S}} \operatorname{div}(\widehat{\mathbf{d}})\mathbf{I} + \mu_{\text{S}}(\nabla \widehat{\mathbf{d}} + \nabla \widehat{\mathbf{d}}^T).$$

The Lamé coefficients λ_{S} and μ_{S} and the structure density ρ_{S} are piecewise constant to account for the different materials in the LZ and SLC:

$$\lambda_{\text{S}} = \begin{cases} \lambda_{\text{LZ}} & \text{in } \Omega_{\text{LZ}} \\ \lambda_{\text{SLC}} & \text{in } \Omega_{\text{SLC}}, \end{cases} \qquad \mu_{\text{S}} = \begin{cases} \mu_{\text{LZ}} & \text{in } \Omega_{\text{LZ}} \\ \mu_{\text{SLC}} & \text{in } \Omega_{\text{SLC}}, \end{cases} \qquad \rho_{\text{S}} = \begin{cases} \rho_{\text{LZ}} & \text{in } \Omega_{\text{LZ}} \\ \rho_{\text{SLC}} & \text{in } \Omega_{\text{SLC}}. \end{cases}$$

Although the landing zone is a biological tissue and thus should, in principle, be modeled as a non-linear hyperelastic material, we assume that the fibrosis and calcium deposits that it bears yield small deformations of the structure, thus justifying a linearized approach. Due to the linearity of the structures, we consider the reconstructed end-diastolic geometry as the reference frame for the structural problem. Indeed, considering a no-stress configuration would only affect the results as an addition of a constant value representing the aortic diastolic pressure, homogeneously in the domain.

For the time discretization of the FSI problem (4) we employ a semi-implicit backward Euler scheme for the fluid problem and a first order implicit scheme for the structure problem. The geometric and kinematic interface coupling are enforced in an essential way, while the continuity of stress between the fluid and the structure is imposed by Lagrange multipliers[36,37]. Space approximation is obtained by piecewise linear finite elements for all the unknowns of the problem, with a SUPG-PSPG stabilization of the fluid subsystem[38,39]. The resulting algebraic system is non-linear due to the implicit treatment of the geometric coupling and for this reason it is solved by an inexact Newton method[40,41], with a FSI-specific monolithic block preconditioner[36,41].

The numerical method described above is implemented in LifeV[42], a parallel finite element library developed in C++ at MOX-Politecnico di Milano, INRIA-Paris, CMCS-EPF of Lousanne, and Emory University-Atlanta, and extensively employed in cardiovascular clinical applications (see, e.g.,[43,44,45,46]), in particular with the described strategy for FSI (see[47,48]).

2.4 | Boundary conditions and simulations settings

Under the assumptions presented at the beginning of Section 2, our simulations consider only the systolic phase of a single heartbeat.

The solid structure is fixed by homogeneous Dirichlet conditions on the external walls $\Sigma_{\text{LZ}}^{\text{wall}}$ and $\Sigma_{\text{SLC}}^{\text{wall}}$, as we neglect the forces exerted by the myocardium during systolic contraction.

For the fluid domain, a time-dependent uniform velocity profile is imposed at the inlet section $\Sigma_{\text{F}}^{\text{in}}$, with a physiological flowrate obtained from[33] and displayed in Fig. 2, right: using this data for all the patients allows a fair comparison among them,

	ρ	E	ν	λ	μ
Landing Zone	$1.1 g/cm^3$	$4 MPa$	0.45	$12.4 MPa$	$1.37 MPa$
SLC	$1.66 g/cm^3$	$8 GPa$	0.3	$4.6 GPa$	$3.08 GPa$

TABLE 1 Mechanical properties of the two structures.

since the size of the prosthesis is the same in all cases, and does not require patient-specific post-intervention data. FSI occurs only with the SLC and LZ, so that the aortic wall is considered rigid and at the outflow section we set homogeneous stress conditions. More refined outlet conditions, such as those based on Windkessel models, were not considered because they would require suitable parameter calibration and, in any case, would not affect the pressure gradients.

Regarding the mechanical properties of the structures, for the LZ we use the values of calcified leaflets as in the work of[8], which corresponds to an intermediate stiffness between physiological leaflets and pure calcifications (see[4]). For the SLC, we consider its stiffness and density to be mainly determined by its metallic component. Since the SLC does not have the porous structure of the actual stent, we scale the mechanical properties of the chrome-cobalt alloy to account for the holes, by analogy with Gibson's trabecular bone model[49]:

$$E_{\mathrm{SLC}} = (1-\Phi)^2 E_{\mathrm{CrCb}}, \qquad \rho_{\mathrm{SLC}} = (1-\Phi)\rho_{\mathrm{CrCb}}, \tag{5}$$

where $\Phi = 0.2$ is the porosity of the actual stent, E_{SLC} and ρ_{SLC} are Young's modulus and the density of the SLC, and E_{CrCb} and ρ_{CrCb} those of the metal. In Table 1 we report the resulting mechanical and physical properties of the two structures, while for blood we consider a density $\rho_{\mathrm{F}} = 1060$ g/cm^3 and viscosity $\mu_{\mathrm{F}} = 0.035$ Poise.

In the mesh generation phase of our reconstruction procedure, we consider a non-homogenous tetrahedralization: the average element size is 0.7 mm in the SLC, 0.5 mm in the LZ, while in the fluid domain it ranges between 0.5 mm in the aortic root to 1.25 mm in the distal region. A time-step of $\Delta t = 0.1$ ms is employed.

2.5 | Outputs of interest

Using the computational model described above, we compared the scenarios associated with the different patients in terms of the following quantities:

- blood velocity distribution in the fluid domain;
- transvalvular pressure drop $\Delta_v p$ between the inlet and the sinotubular junction section. This is one of the main quantities of interest in the clinical assessment of a prosthetic valve and in follow-up evaluations;
- Wall Shear Stress (WSS) exerted by the fluid on the aortic wall:

  $$WSS = \mathbf{T}_{\mathrm{F}}\,\mathbf{n} - (\mathbf{T}_{\mathrm{F}}\,\mathbf{n})\cdot\mathbf{n},$$

  where $\mathbf{n}$ is the normal versor. The distributions of this surface field and of its time average

  $$TAWSS = \frac{1}{T}\int_0^T WSS\, dt.$$

  are associated with different vascular diseases, in particular calcification and atherosclerosis[50];
- WSS and TAWSS critical areas:

  $$\begin{aligned} A^{\mathrm{peak}}_{WSS} &= \text{ area of } \{\mathbf{x}\in\Sigma^{\mathrm{wall}}_{\mathrm{F}} :\ |WSS(t_{\mathrm{peak}},\mathbf{x})| > 1 \text{ Pa}\},\\ A_{TAWSS} &= \text{ area of } \{\mathbf{x}\in\Sigma^{\mathrm{wall}}_{\mathrm{F}} :\ |TAWSS(\mathbf{x})| > 0.5 \text{ Pa}\}, \end{aligned} \tag{6}$$

  where t_{peak} is the time corresponding to the systolic peak. These areas are expressed as a percentage of the total area of the fluid domain wall $\Sigma^{\mathrm{wall}}_{\mathrm{F}}$. The threshold values of 1 Pa and 0.5 Pa employed in definition (6) identify areas of higher (albeit not necessarily pathological) WSS. Notice that physiological values for peak-systole WSS near the sinotubular junction range between 0.3-0.6 Pa, as reported, e.g., in[51];

	Native Orifice Area	Equivalent Orifice Diameter	Mean Vessel Radius
NODEG1	4.05cm^2	2.27cm	1.84cm
NODEG2	5.83cm^2	2.73cm	1.97cm
DEG1	3.47cm^2	2.10cm	1.60cm
DEG2	3.40 cm^2	2.08cm	1.68cm
DEG3	4.41cm^2	2.37cm	1.69cm

TABLE 2 Clinical measures for the five patients: area of the native annulus, equivalent orifice diameter computed (assuming the native orifice to be a circle) and mean radius of the ascending aorta.

- Von Mises equivalent stress (σ_{VM}) in the annulus, representative of the stresses generated within the structure:

$$\sigma_{VM} = \sqrt{\frac{(\mathbf{T}_{\mathrm{S11}} - \mathbf{T}_{\mathrm{S22}})^2 + (\mathbf{T}_{\mathrm{S22}} - \mathbf{T}_{\mathrm{S33}})^2 + (\mathbf{T}_{\mathrm{S11}} - \mathbf{T}_{\mathrm{S33}})^2 + 6(\mathbf{T}_{\mathrm{S12}}^2 + \mathbf{T}_{\mathrm{S23}}^2 + \mathbf{T}_{\mathrm{S13}}^2)}{2}}.$$

3 | RECONSTRUCTION PROCEDURE: RESULTS AND DISCUSSION

As described in Section 2.2 - Step 2, our virtual implantation procedure encompasses the enlargement of the annulus, which is the virtual counterpart of the balloon expansion performed during the clinical procedure, to break the calcifications and ensure a complete opening of the stent up to its nominal dimensions. Among the 5 patients considered, only NODEG2 did not need a virtual expansion of the annulus, as we can see from Fig. 3 - above: the native dimensions of the annulus of NODEG2 are large enough to contain the SLC. This is consistent with the clinical measurements reported in Table 2: NODEG2 has the largest orifice area, and the equivalent orifice diameter is larger than the sum of the prosthesis external diameter (23 mm) and the typical 4 mm thickness of calcified leaflets [32]. On the other hand, the native orifice areas of DEG1 and DEG2 – which are comparable to one another – are the smallest among the patients under investigation, and thus their annuli needed to be enlarged the most. This observation is consistent with the conjecture that a reduced pre-operative area of the aortic annulus w.r.t. to the size of the prosthesis is one of the factors that may lead to SVD, as formulated in the CAVEAT study [13].

As mentioned in Section 2.2, the same SAPIEN XT prosthesis is implanted in all patients, thus the SLC has the same dimension in all cases. However, its positioning in the orifice plane is affected by the patient-specific distribution of pre-implantation calcium deposits, as described in Section 2.2 - Step 3. In Fig. 3, above, we show how the distance between the annulus centerline and the position of the SLC obtained after its positioning procedure highly differs among the patients. In particular, we notice that little displacement is performed in the cases of NODEG2 and DEG3, where the calcium distribution is essentially uniform in the circumferential direction, while the largest displacement is attained for DEG1, where such distribution is more concentrated on the left side of the annular plane.

From Fig. 3 we also notice how pre-implantation calcium deposits are the largest in DEG3. This may suggest that this patient is significantly prone to leaflets calcifications.

At the end of the virtual insertion, we verified that the downstream end of the SLC is upstream w.r.t. the coronary ostia for all the patients at hand, as indicated by implantation guidelines [52] to prevent the stent structure from impairing coronary perfusion. In the case of DEG1 and DEG3, we could also compare our geometries (reconstructed using only *pre*-implantation data) with 1-year follow-up CT scans, noticing that our virtual balloon expansion yields a good geometric agreement with this imaging data, both in the ascending aorta and in the Valsalva sinuses, as shown in Fig. 4. Moreover, we noticed that the implanted stent actually attained its nominal diameter of 23 mm and had a circular section.

4 | FSI ANALYSIS: NUMERICAL RESULTS AND DISCUSSION

The FSI problem described in Section 2.3 is solved by the finite element library LifeV [42]. We performed a convergence analysis w.r.t. space and time discretization, at the end of which we chose $h_{\max} = 1.25$ mm as characteristic finite element size and $\Delta t = 0.1$ ms as time step. In Table 3, we summarize the mesh convergence analysis for patient NODEG2: each mesh is identified

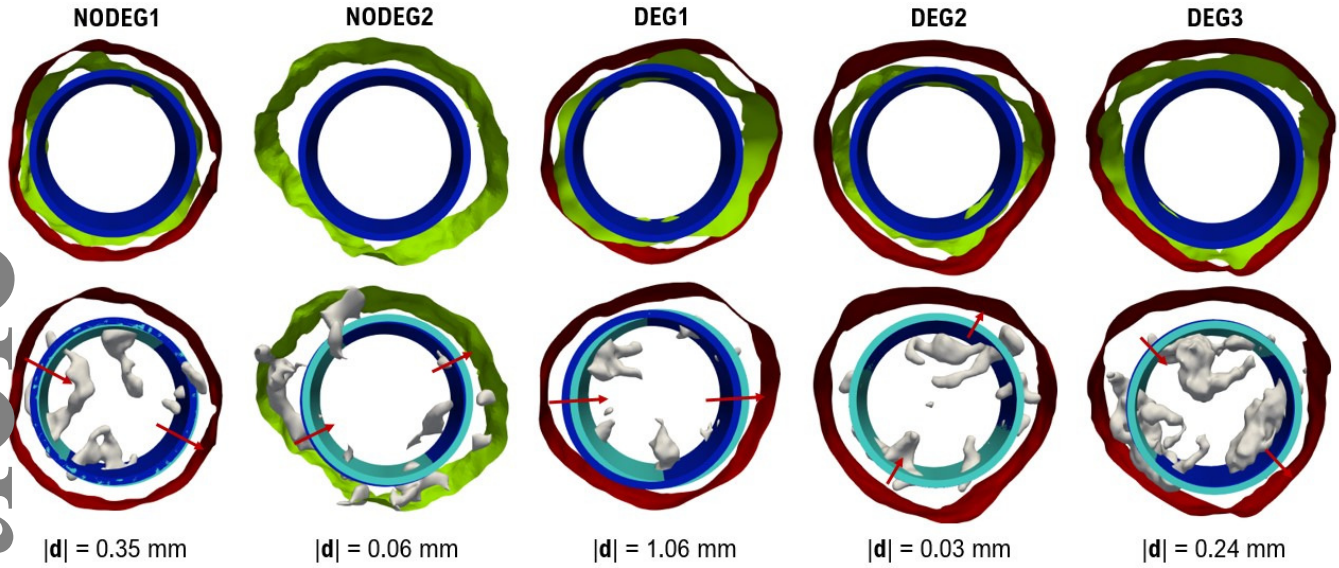

FIGURE 3 Artificial enlargement of the annulus (Step 2) and stent positioning (Step 3). Above: the segmented annulus (green) is expanded as in Step 2 of the reconstruction procedure; the expanded annulus is depicted in red (patient NODEG2 did not require expansion) and the SLC, positioned on the vessel centerline, is reported in blue for comparison. Below: based on the distribution of calcium deposits (gray) the SLC is displaced from its position on the centerline (dark blue) to a new position (light blue) by a displacement **d** (direction in red arrows) as in Step 3 of the reconstruction procedure; the (possibly) expanded annulus trace is reported for reference.

$h_{\max}$ (mm)	N	$e^{\Delta_v p}$	$e^{WSS,\text{mid}}$	$e^{WSS,\text{top}}$	$e^{\sigma_{VM},\text{left}}$	$e^{\sigma_{VM},\text{right}}$
5	347k	-	-	-	-	-
2.5	484k	0.032	0.012	0.020	1.216	1.304
1.25	660k	0.003	0.017	0.006	0.014	0.138

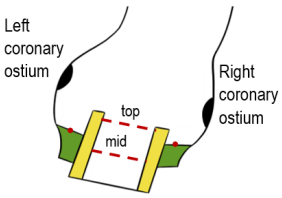

TABLE 3 Mesh convergence analysis: $h_{\max}$ is the maximum edge length, N is the number of tetrahedra of the volumetric mesh and the expression for the relative differences e^{ψ} is defined in (7). $\Delta_v p$ is the transvalvular pressure drop, WSS is averaged on the two circumferences on the inner stent wall depicted in the schematic representation on the right, σ_{VM} values are computed at two points of the annulus interface, in the left and right coronary sinuses.

by its $h_{\max}$, and we report the relative difference of some representative quantities between different levels of refinement: for a quantity of interest $\psi(h_{\max})$, the relative difference e^{ψ} is defined as

$$e^{\psi} = \left| \frac{\psi(h_{\max}) - \psi(2\,h_{\max})}{\psi(2\,h_{\max})} \right|. \tag{7}$$

As shown in Table 3, the choice of $h_{\max} = 1.25$ mm ensures a mesh sensitivity to further refinements of less than 2% on the transvalvular pressure drop and representative values of WSS and σ_{VM}.

Each simulation required a wall time of about 70 hours on a HPC node with 32 processors Intel(R) Xeon(R) E5-4610 and 1.2 TB RAM.

4.1 | Fluid dynamics analysis

In Fig. 5 we report the velocity field for all patients at the systolic peak and during the deceleration phase. The velocity attains its maximum at the systolic peak, downstream the SLC, with a value of 1.5 m/s laying in the physiological range, in accordance

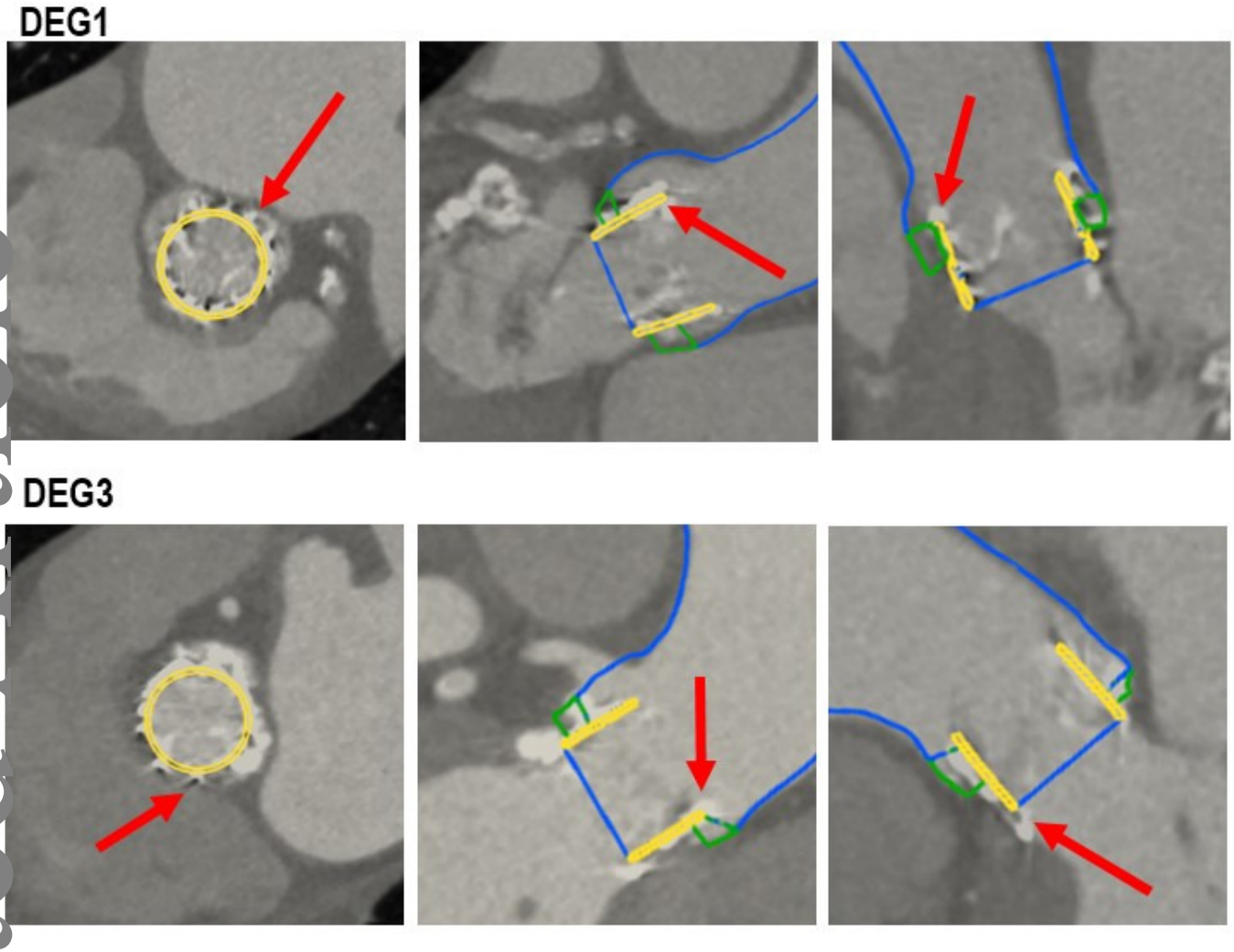

FIGURE 4 Comparison of the reconstructed geometries (yellow: SLC; green: LZ; blue: fluid domain) with 5-year follow-up CT scans of patients DEG1 (above) and DEG3 (below). The stent in the background grayscale CT image can be identified by the alternate white-black regions (see the red arrows).

with the literature[53,54]. We observe the typical jet flow, impinging on the extrados of the ascending aorta, as well as late-systolic recirculation patterns in the intrados region. The jet covers a larger portion of the computational domain in the cases DEG1 and DEG2, in comparison with NODEG1 and NODEG2, while in the DEG3 case its impingement on the outer wall is stronger due to the rapid bending of the geometry. Accordingly, the largest recirculation vortex is centered near the point of maximum curvature in the NODEG cases, whereas it is displaced downstream in DEG1 and DEG2, since the wider jet prevents its formation in the proximal region of the domain; regarding DEG3, instead, the rapid deviation of the geometry w.r.t. the direction of the jet leaves room for the formation of a recirculation structure very near to the aortic root.

From Fig. 5 we also notice that two of the degenerate cases (DEG1 and DEG3) have a significantly more pronounced curvature with respect to the non-degenerate case, resulting in a strong divertion of the systolic jet. This geometrical observation will have a role also in the discussion on the wall shear stress.

In Fig. 6, we can observe that the overall pressure drop between the inlet and the outlet sections is about 3 mmHg at the systolic peak for all the patients. For the DEG patients, higher values of pressure drop (around 2 mmHg) w.r.t. the NODEG patients are reached in localized areas near the extrados of the aorta. This is consistent with the previous comment about the more pronounced vessel curvature of DEG1 and DEG3. However, since the high-pressure areas are different for each patient, the pressure distribution at the systolic peak does not provide relevant indices associated to SVD. Similarly, in the deceleration

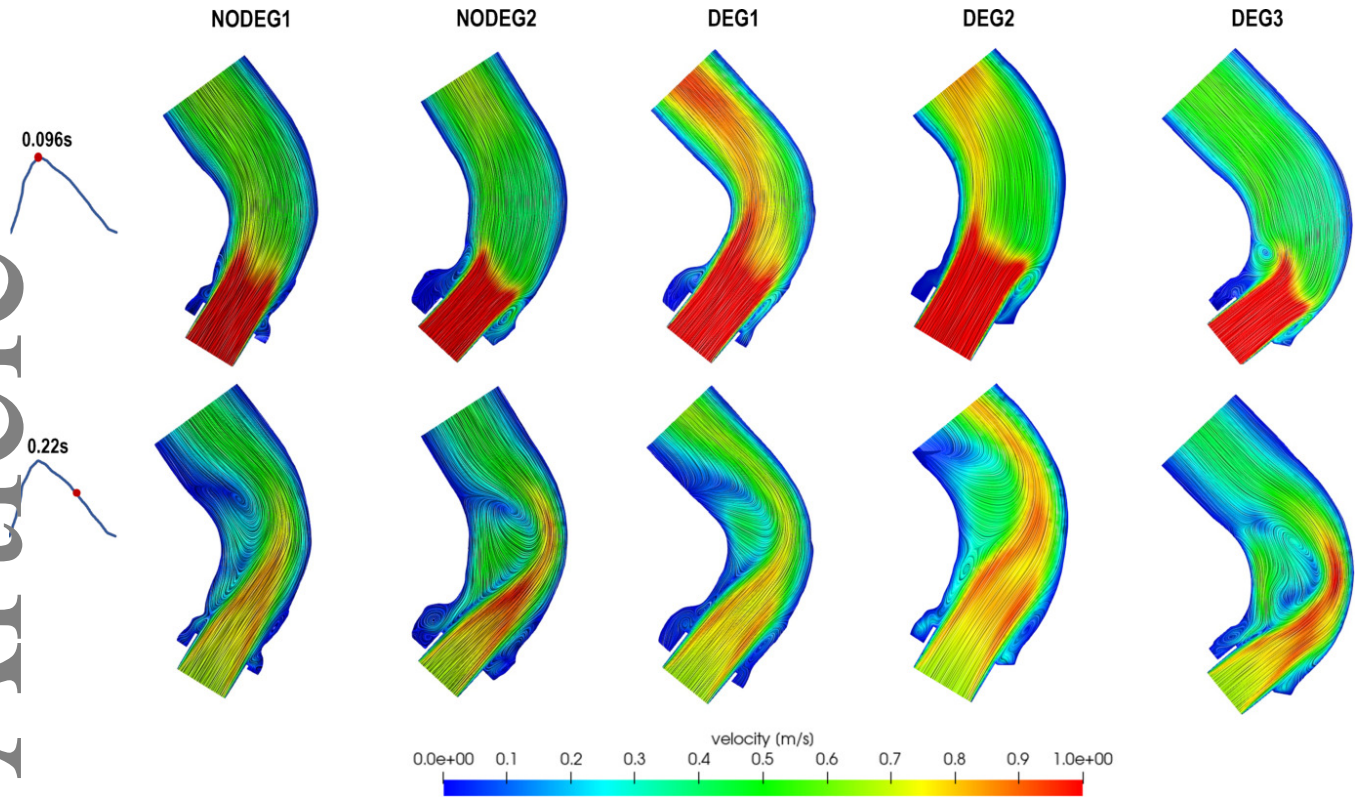

FIGURE 5 Velocity field on a transversal slice at the systolic peak (above) and during the deceleration phase (below), for the five patients. On the left, the selected time instants identified on the inlet flowrate curve.

phase, some differences can be observed in the pressure distribution of the different patients, but no significant distinction between the DEG and NODEG cases is appreciated.

In Fig. 7 we report the WSS spatial distribution on the fluid domain wall of all patients, at the systolic peak. For all the patients, we notice high stress on the inner SLC wall, due to the drag force exerted on the prosthesis, while small stress values are attained in the Valsalva sinuses, especially in the right and left coronary sinuses. To quantify the differences between the patients, we define thresholds of 1 Pa and 0.5 Pa for WSS and TAWSS, respectively. Such values were selected to highlight the differences between DEG and NODEG patients. In fact, we are proposing such thresholds as a new way to discriminate TAVI patients w.r.t. prosthesis degeneration. Notice that the threshold of 1 Pa is higher than the average physiological peak values of WSS near the sinotubular junction, which have been found to be around 0.5 Pa (see, e.g.,[51]). It is worth to point out that stress values above these thresholds are not pathological *per se*: they simply show good correlation with the classification as DEG or NODEG for the patients under investigation.

Differences in WSS among the patients can be observed donwstream to the sinotubular junction. For example, in DEG1, high stresses are assumed on the intrados of the aortic wall, while for the other patients the highest values of WSS are attained on the extrados. The main difference, however, lays in the amount of aortic wall interested by high values of viscous stress. In particular, in the NODEG cases the WSS is lower than 1 Pa in most of the ascending aorta, while for the DEG patients large portions of the wall present high values of WSS. To quantify these differences, we compute the *WSS critical area* A^{peak}_{WSS}, that is the area of the region in which $|WSS| > 1$ Pa at the systolic peak (see (6)). The values for such area are reported in Table 4 as a fraction of the total area of the ascending aorta. Consistently with the comments above, the NODEG patients present a smaller value of A^{peak}_{WSS} than the DEG ones, especially if considering the large values obtained for DEG1 and DEG3, confirming that this parameter can be a significant indicator for SVD prediction.

In Fig. 7 we also report the time evolution of the average WSS computed over a region located between the sinotubular junction and the point of maximum deviation of the aortic centerline (see scheme in Fig. 7, top right), which contain the WSS critical areas of all the patients. We observe that the DEG cases are characterized by time-persistent values of such space-averaged WSS over 0.5 Pa, especially in the early systolic phase, whereas in the NODEG cases this spatial average remains

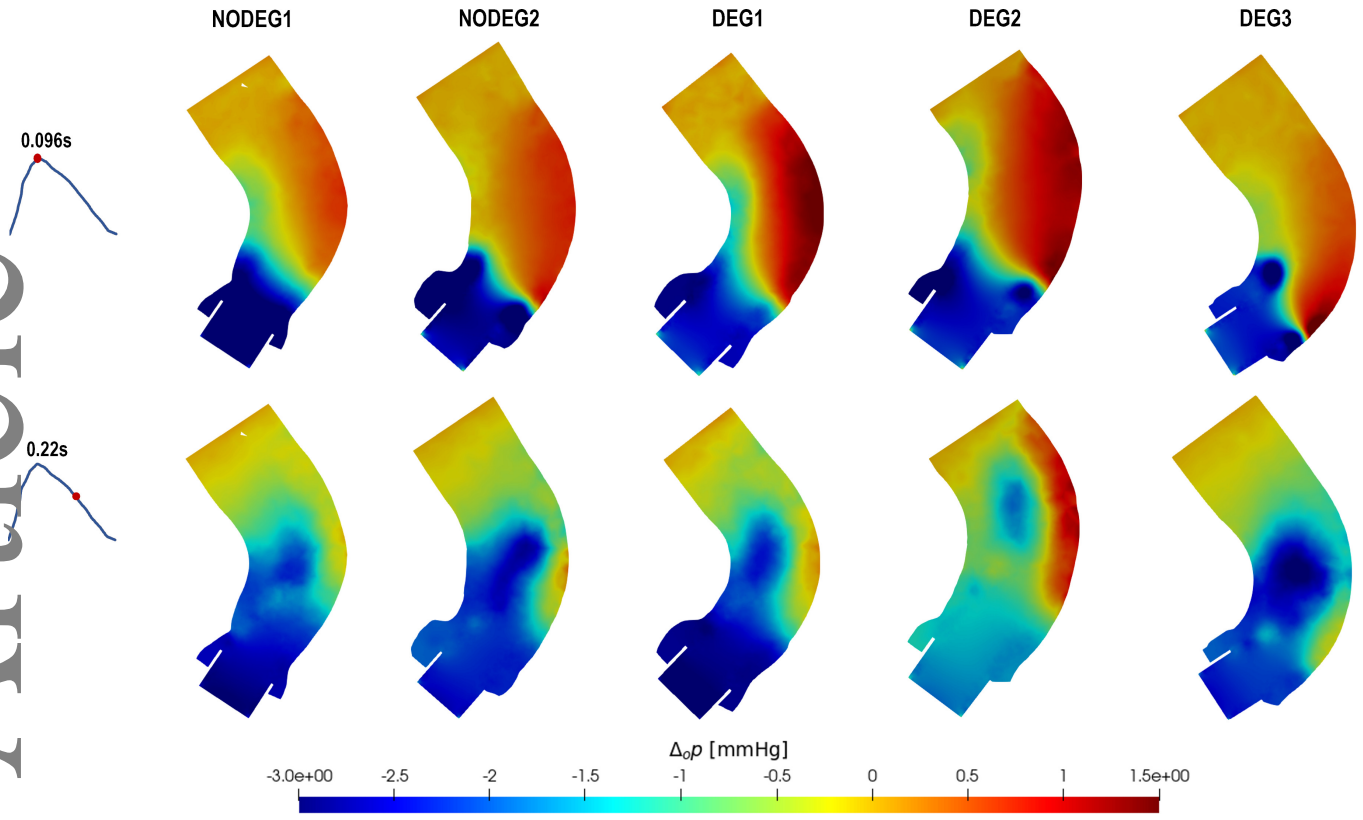

FIGURE 6 Pressure gradient w.r.t. the outlet on a transversal slice at the systolic peak (above) and during the deceleration phase (below), for the five patients. On the left, the selected time instants identified on the inlet flowrate curve.

	WSS critical area $A^{\text{peak}}_{WSS}/\lvert\Sigma^{\text{wall}}_{\text{F}}\rvert$ [%]	$TAWSS$ critical area $A_{TAWSS}/\lvert\Sigma^{\text{wall}}_{\text{F}}\rvert$ [%]
NODEG1	0.50%	1.34%
NODEG2	2.15%	1.31%
DEG1	5.38%	5.84%
DEG2	2.37%	3.50%
DEG3	4.85%	13.95%

TABLE 4 Area of the critical regions in which $|WSS| > 1$ Pa (at the systolic peak) and $|TAWSS| > 0.5$ Pa, respectively, expressed as percentages of the total area of the aortic wall $\Sigma^{\text{wall}}_{\text{F}}$.

below the threshold, except for very short times. This observation is relevant because concentrated and time-persistent high values of WSS like those observed in the DEG patients have two implications: first, they may be a factor of possible damage to the endothelial tissue of the aortic wall; second, they can be interpreted as indicators of reduced compatibility between the implantation site and and the BHV, thus possibly foretelling the onset of SVD.

To synthesize the time evolution of the viscous stress, in Fig. 8 we report the distribution of $TAWSS$ on the aortic wall. Both DEG1 and DEG3 present higher values of $TAWSS$ with respect to the other patients, localized in the same regions that were identified for the WSS (see Fig. 7). A quantitative measure of such regions is represented by the *TAWSS critical area* A_{TAWSS} where $|TAWSS| > 0.5$ Pa. The values of such area are reported in Table 4: all the DEG subjects present a larger high-value region than the NODEG cases, confirming this parameter to be relevant in the prediction of SVD. Actually, A_{TAWSS} proves to be even better at discriminating between DEG and NODEG cases, with respect to A^{peak}_{WSS}, suggesting its relevance as a predictive indicator for SVD.

To complete the analysis of the fluid dynamics results, we report that we investigated also the time evolution of the transvalvular pressure drop $\Delta_v p$. However, no significant differences could be observed among the five patients under study, and a maximum

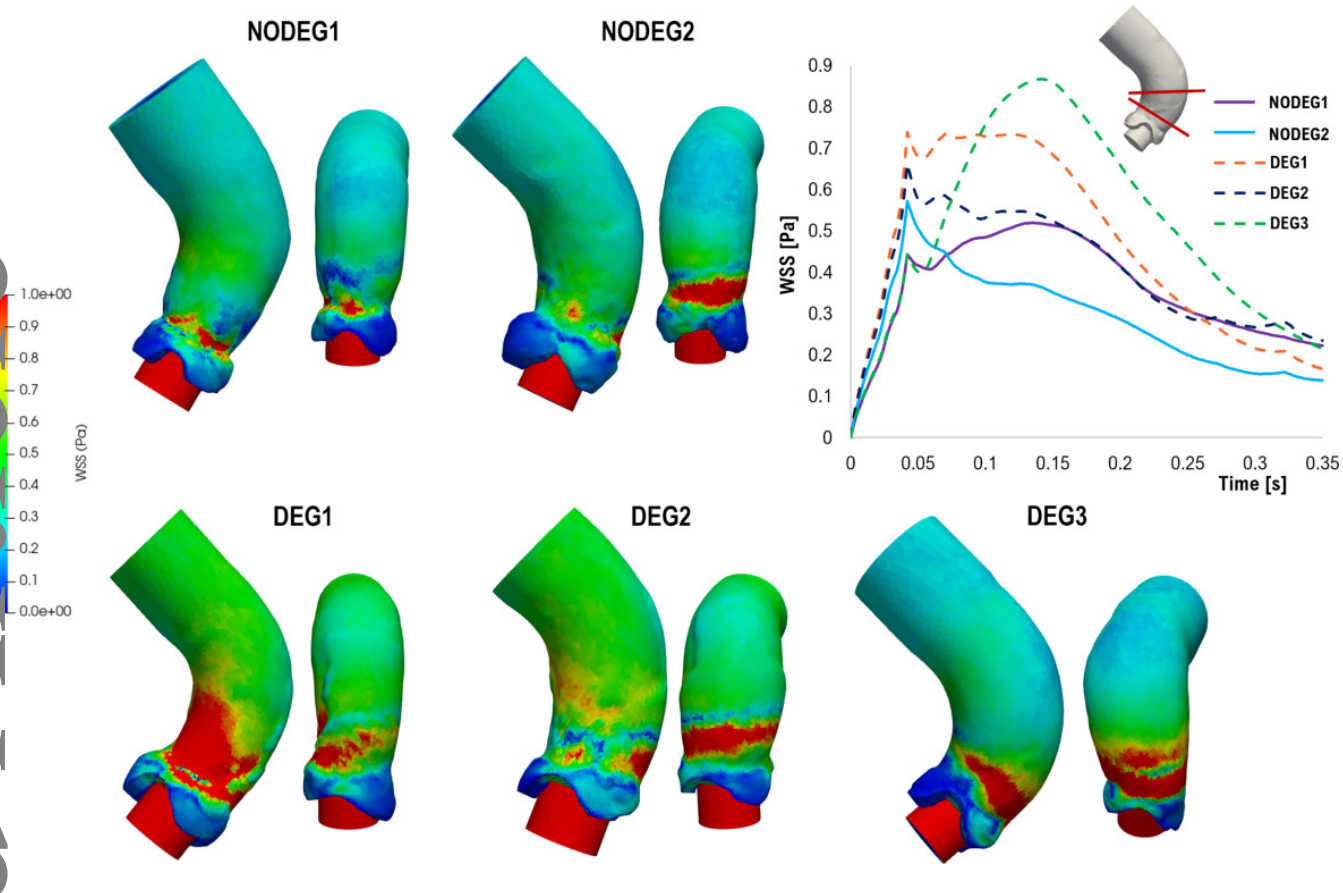

FIGURE 7 WSS distribution on the internal wall of the SLC and on the aortic wall at the systolic peak ($t = 0.096$ s). Top-right corner: time evolution of the mean WSS on the region between the sinotubular junction and the point of maximum deviation of the aortic centerline, as depicted by the two red lines in the scheme above.

value of $\Delta_v p \in [5.5, 6.5]$ mmHg – within the physiological range [5, 11] mmHg[54] – was attained in all cases. Our results are in contrast with the clinical practice that considers the transvalvular pressure drop as a widely employed quantity for the assessment of prosthetic valves function, since it is routinely measurable by Doppler echocardiography. For this reason, further investigation in this direction will be mandatory. Indeed, the lack of differences between the patients investigated can be ascribed to the fact that the same prosthesis and inflow conditions have been considered for all of them, while variability on the actual shape and size of the prosthesis and on the cardiac output has to be considered in the clinical practice.

4.2 | Structural analysis

To fully exploit the FSI nature of the problem, we report and discuss the results obtained on the displacements and stresses undergone by the structural components of the system, namely the SLC and the LZ.

In all cases, the displacement of the SLC is mainly radial, since the fixed boundary condition on the inlet base of the stent prevents motion along the flow direction, while the LZ is essentially directed in the flow direction, because of both the rigid-wall assumption on the aortic wall and the action of the recirculating flow in the Valsalva sinuses, which creates a low-pressure region pulling downstream the LZ. However, all such displacements are of the order of μm, and negligible differences are observed among the patients.

From the viewpoint of the forces exerted on the structure, in Fig. 9 we report the Von Mises stress distribution on the landing zone during the acceleration phase of the systole ($t = 0.042$ s). We can notice that the larger stresses are attained at the interfaces with the aortic wall and the SLC, due to the linear elasticity assumption, but no relevant characteristics allow to discriminate between the NODEG and DEG clinical samples.

Summarizing, we can state that no structural indicators were identified for the prediction of SVD.

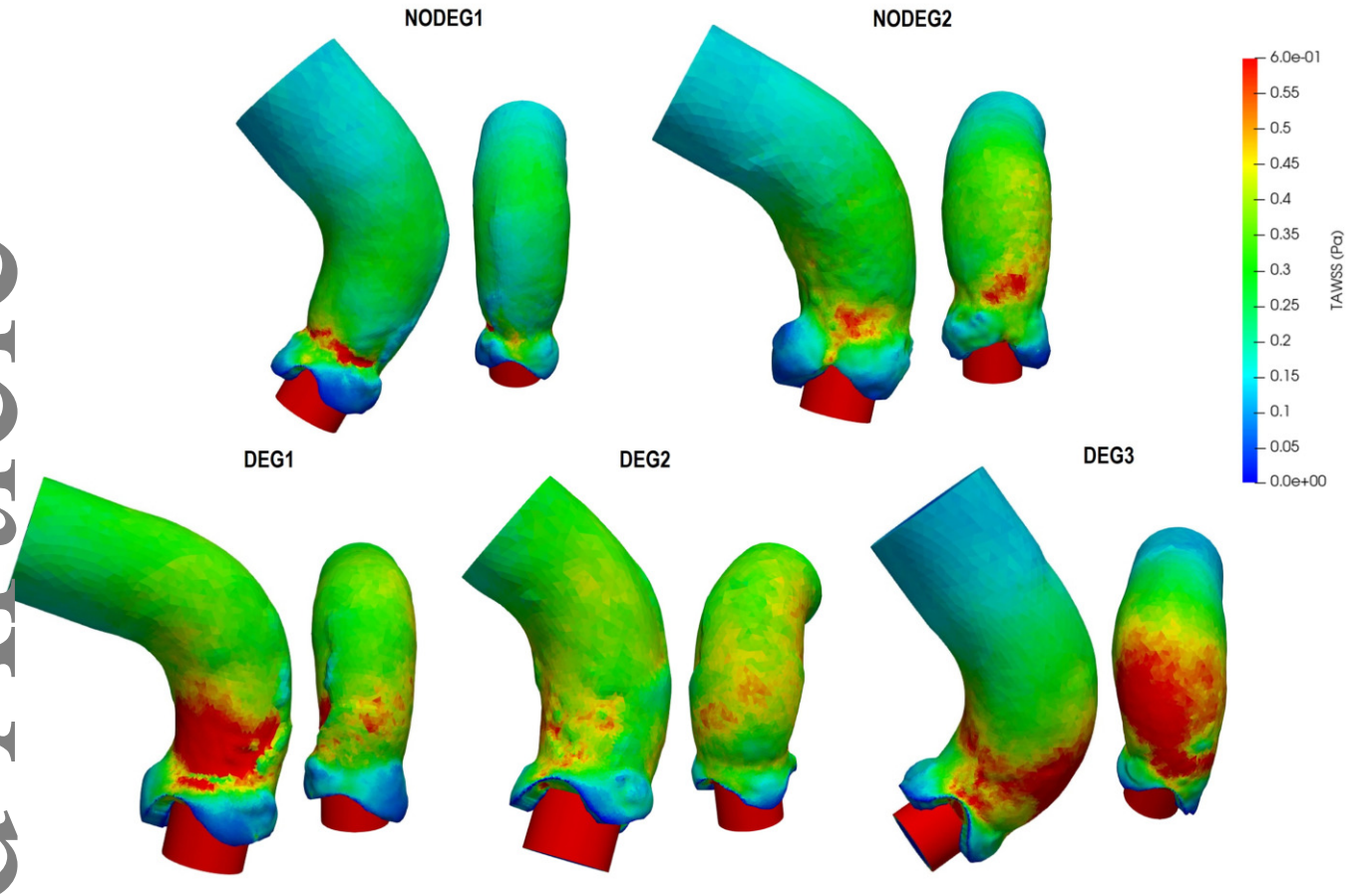

FIGURE 8 $TAWSS$ distribution on the internal wall of the SLC and on the aortic wall.

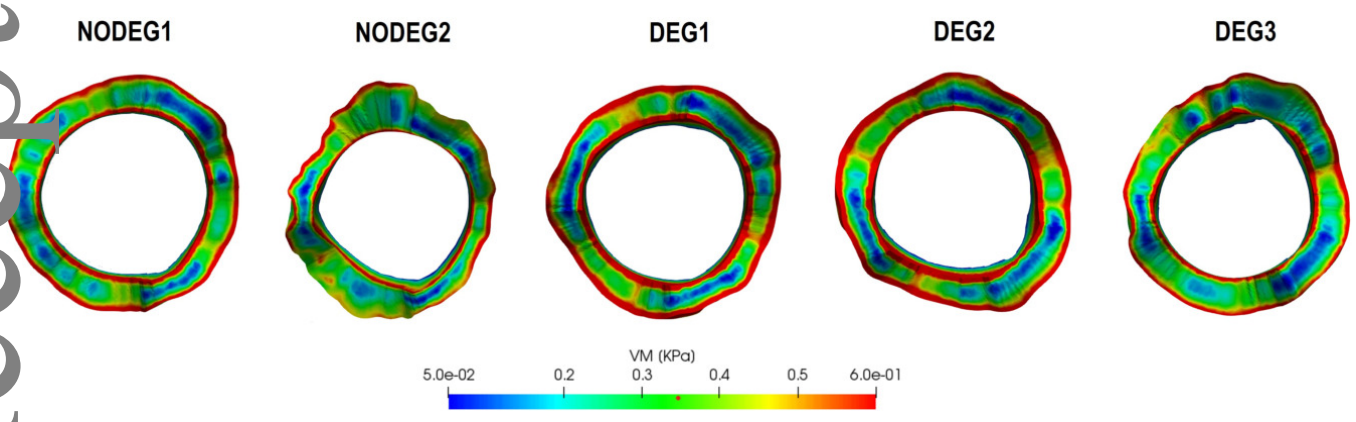

FIGURE 9 VM stress distribution at early-systole instant (0.042s) over the downwind surface of the landing zone.

5 | FINAL REMARKS AND LIMITATIONS

We investigated the systolic hemodynamics in the aorta of five patients that underwent TAVI and whose follow up at 5-10 years from the implant is known. We built a FSI model of the TAVI implant with the aim of identifying predictive indicators for the onset of SVD based onto the knowledge of only pre-operative information. We compared the different patients in terms of the outcomes of the reconstruction procedure and of the FSI simulations to identify indicators that could discriminate between

the patients who suffered from SVD (DEG patients) in a 5-10 year timespan and those whose prosthesis did not degenerate (NODEG).

The main outcomes of this study are the following:

1. We confirmed some literature observations indicating a reduced native orifice area and widely calcified native leaflets as possible risk factors.
2. On the other hand, we observed that the transvalvular pressure drop, which is routinely measured in the assessment of prosthetic valves function, is not a significant indicator for SVD prediction.
3. We identified other SVD-predictive quantities that cannot be directly measured by diagnostic tests. In particular, we observed a difference in the position of the main recirculation vortex in late systole, between the NODEG and DEG patients, and we noticed even more significant differences in the viscous stress exerted by the blood flow on the proximal region of the ascending aorta: the DEG patients are characterized by larger and time-persistent values of WSS, especially in the early systole, and by wider regions of high stress on the aortic wall at the systolic peak.
4. The quantity that proved to be the best at discriminating between the DEG and NODEG patients samples is the TAWSS critical area A_{TAWSS}, namely the area of the region where the TAWSS exceeds a threshold of 0.5 Pa.
5. In the settings considered in this work, a purely CFD analysis – that is with all the structures modeled as rigid – would have likely yielded comparable results. Although this can be useful for reducing the computational cost of the simulations, an a priori justification for this choice can be difficult and controversial: the results of our FSI analysis are obtained without assuming rigidity of the prosthesis and of the tissue surrounding it.

This study presents the following limitations:

1. Unlike for the stent-leaflets complex, we considered the aortic wall as rigid and prescribed a fixed position of the stent inlet, thus neglecting the forces exerted on the SLC and LZ by the elastic vessel wall and the contracting ventricle. In this direction, more refined boundary conditions, such as absorbing or Windkessel at the outlet[55], should be suitably considered.
2. We modeled the stent and the adhering leaflets as a single structure. Removing this assumption and that of point 1 may have an impact on the forces exchanged among the different structural and anatomical components, thus possibly leading to the identification of additional predictive indicators for SVD. Moreover, this separation of the leaflets from the stent may improve the accuracy of the model in the description of the early stages of the systolic and diastolic phases, by allowing to also investigate the effects of the geometry and motion of the leaflets explicitly, and possibly observe degeneration factors on their tissue.
3. The LZ is considered as a homogeneous mixture of physiological leaflet tissue and calcium deposits: future work may consider a heterogeneous distribution of the calcifications, in order to study the effects of such heterogeneity on the device implantation and on its degeneration.
4. Our investigation focused on the sole systolic phase, thus it did not analyze the effects of the pressure gradients across the closed valve and the recirculation flows sliding on the aortic side of the prosthetic leaflets. The determination of diastolic indicators could then be the subject of future research.
5. The promising results that we obtained should be verified on a larger set of patients, in order to provide statistical significance and validation to our observations. Moreover, finding a way to predict the cardiac output and boundary conditions of a subject after the intervention (though still based on just pre-implantation data) would allow to better analyze the patients' specific conditions.

Despite these limitations, the current study represents the first patient-specific computational investigation on the prediction of SVD onset, which paves the way to more detailed analyses and to the definition of a clinical score that may help the clinician both in the design of the TAVI procedure and in the post-implantation monitoring of the patient.

ACKNOWLEDGMENTS

This project has received funding from the European Research Council (ERC) under the European Union's Horizon 2020 research and innovation programme (grant agreement No 740132, iHEART 2017-2022, P.I. A. Quarteroni).

References

1. Schoen FJ. Cardiac valves and valvular pathology: update on function, disease, repair, and replacement. *Cardiovascular Pathology* 2005; 14(4): 189–194.
2. Schwarz F, Baumann P, Manthey J, et al. The effect of aortic valve replacement on survival. *Circulation* 1982; 66(5): 1105–1110.
3. Vahanian A, Alfieri O, Andreotti F, et al. Guidelines on the management of valvular heart disease (version 2012): the joint task force on the management of valvular heart disease of the European Society of Cardiology (ESC) and the European Association for Cardio-Thoracic Surgery (EACTS). *European Heart Journal* 2012; 33(19): 2451–2496.
4. Vy P, Auffret V, Badel P, et al. Review of patient-specific simulations of transcatheter aortic valve implantation. *International Journal of Advances in Engineering Sciences and Applied Mathematics* 2016; 8(1): 2–24.
5. Carroll JD, Mack MJ, Vemulapalli S, et al. STS-ACC TVT registry of transcatheter aortic valve replacement. *Journal of the American College of Cardiology* 2020; 76(21): 2492–2516.
6. Mack MJ, Leon MB, Thourani VH, et al. Transcatheter aortic-valve replacement with a balloon-expandable valve in low-risk patients. *New England Journal of Medicine* 2019; 380(18): 1695–1705.
7. Ghosh RP, Marom G, Bianchi M, D'souza K, Zietak W, Bluestein D. Numerical evaluation of transcatheter aortic valve performance during heart beating and its post-deployment fluid-structure interaction analysis. *Biomechanics and modeling in mechanobiology* 2020; 19(5): 1725–1740.
8. Luraghi G, Migliavacca F, García-González A, et al. On the modeling of patient-specific transcatheter aortic valve replacement: a fluid–structure interaction approach. *Cardiovascular engineering and technology* 2019; 10(3): 437–455.
9. Czerwińska-Jelonkiewicz K, Michałowska I, Witkowski A, et al. Vascular complications after transcatheter aortic valve implantation (TAVI): risk and long-term results. *Journal of thrombosis and thrombolysis* 2014; 37(4): 490–498.
10. Muratori M, Fusini L, Tamborini G, et al. Five-year echocardiographic follow-up after TAVI: structural and functional changes of a balloon-expandable prosthetic aortic valve. *European Heart Journal-Cardiovascular Imaging* 2018; 19(4): 389–397.
11. Kataruka A, Otto CM. Valve durability after transcatheter aortic valve implantation. *Journal of thoracic disease* 2018; 10(Suppl 30): S3629.
12. Kostyunin AE, Yuzhalin AE, Rezvova MA, Ovcharenko EA, Glushkova TV, Kutikhin AG. Degeneration of bioprosthetic heart valves: update 2020. *Journal of the American Heart Association* 2020; 9(19): e018506.
13. Guglielmo M, Fusini L, Muratori M, et al. Computed tomography predictors of structural valve degeneration in patients undergoing transcatheter aortic valve implantation with balloon-expandable prostheses. *European Radiology* 2022: 1–11.
14. Costa G, Criscione E, Todaro D, Tamburino C, Barbanti M. Long-term transcatheter aortic valve durability. *Interventional Cardiology Review* 2019; 14(2): 62.
15. Loureiro-Ga M, Veiga C, Fdez-Manin G, et al. Predicting TAVI paravalvular regurgitation outcomes based on numerical simulation of the aortic annulus eccentricity and perivalvular areas. *Computer Methods in Biomechanics and Biomedical Engineering* 2021: 1–9.

16. Finotello A, Morganti S, Auricchio F. Finite element analysis of TAVI: Impact of native aortic root computational modeling strategies on simulation outcomes. *Medical engineering & physics* 2017; 47: 2–12.

17. Pasta S, Cannata S, Gentile G, et al. Simulation study of transcatheter heart valve implantation in patients with stenotic bicuspid aortic valve. *Medical & biological engineering & computing* 2020; 58(4): 815–829.

18. Bosi GM, Capelli C, Cheang MH, et al. A validated computational framework to predict outcomes in TAVI. *Scientific reports* 2020; 10(1): 1–11.

19. Kopanidis A, Pantos I, Alexopoulos N, Theodorakakos A, Efstathopoulos E, Katritsis D. Aortic flow patterns after simulated implantation of transcatheter aortic valves. *Hellenic J Cardiol* 2015; 56(418): 428.

20. Mao W, Wang Q, Kodali S, Sun W. Numerical parametric study of paravalvular leak following a transcatheter aortic valve deployment into a patient-specific aortic root. *Journal of biomechanical engineering* 2018; 140(10): 101007.

21. Bianchi M, Marom G, Ghosh RP, et al. Patient-specific simulation of transcatheter aortic valve replacement: impact of deployment options on paravalvular leakage. *Biomechanics and modeling in mechanobiology* 2019; 18(2): 435–451.

22. Becsek B, Pietrasanta L, Obrist D. Turbulent systolic flow downstream of a bioprosthetic aortic valve: velocity spectra, wall shear stresses, and turbulent dissipation rates. *Frontiers in physiology* 2020; 11.

23. Luraghi G, Matas JFR, Beretta M, Chiozzi N, Iannetti L, Migliavacca F. The impact of calcification patterns in transcatheter aortic valve performance: a fluid-structure interaction analysis. *Computer Methods in Biomechanics and Biomedical Engineering* 2020: 1–9.

24. Mirsadraee S, Sellers S, Duncan A, Hamadanchi A, Gorog D. Bioprosthetic valve thrombosis and degeneration following transcatheter aortic valve implantation (TAVI). *Clinical Radiology* 2021; 76(1): 73–e39.

25. Todaro D, Picci A, Barbanti M. Current TAVR devices. *Card Intervent Today* 2017; 11: 53–58.

26. Noorani A, Bapat V. Differences in outcomes and indications between Sapien and CoreValve transcatheter aortic valve implantation prostheses. *Interventional Cardiology Review* 2014; 9(2): 121.

27. Antiga L, Piccinelli M, Botti L, Ene-Iordache B, Remuzzi A, Steinman DA. An image-based modeling framework for patient-specific computational hemodynamics. *Medical & biological engineering & computing* 2008; 46(11): 1097–1112.

28. Lorensen WE, Cline HE. Marching cubes: A high resolution 3D surface construction algorithm. *ACM siggraph computer graphics* 1987; 21(4): 163–169.

29. Antiga L, Piccinelli M, Botti L, Ene-Iordache B, Remuzzi A, Steinman DA. An image-based modeling framework for patient-specific computational hemodynamics. *Medical & biological engineering & computing* 2008; 46(11): 1097–1112.

30. Antiga L, Ene-Iordache B, Remuzzi A. Computational geometry for patient-specific reconstruction and meshing of blood vessels from MR and CT angiography. *IEEE transactions on medical imaging* 2003; 22(5): 674–684.

31. Meyer M, Desbrun M, Schröder P, Barr AH. Discrete differential-geometry operators for triangulated 2-manifolds. In: Springer. 2003 (pp. 35–57).

32. Cheng CL, Chang HH, Huang PJ, Wang WC, Lin SY. Ex vivo assessment of valve thickness/calcification of patients with calcific aortic stenosis in relation to in vivo clinical outcomes. *Journal of the mechanical behavior of biomedical materials* 2017; 74: 324–332.

33. Capellini K, Vignali E, Costa E, et al. Computational fluid dynamic study for aTAA hemodynamics: an integrated image-based and radial basis functions mesh morphing approach. *Journal of biomechanical engineering* 2018; 140(11).

34. Quarteroni A, Manzoni A, Vergara C. The cardiovascular system: mathematical modelling, numerical algorithms and clinical applications. *Acta Numerica* 2017; 26: 365–590.

35. Donea J, Giuliani S, Halleux JP. An arbitrary Lagrangian-Eulerian finite element method for transient dynamic fluid-structure interactions. *Computer methods in applied mechanics and engineering* 1982; 33(1-3): 689–723.

36. Deparis S, Forti D, Grandperrin G, Quarteroni A. FaCSI: A block parallel preconditioner for fluid-structure interaction in hemodynamics. *Journal of Computational Physics* 2016; 327: 700–718.

37. Veneziani A, Vergara C. Flow rate defective boundary conditions in haemodynamics simulations. *International Journal for Numerical Methods in Fluids* 2005; 47(8-9): 803–816.

38. Tezduyar TE. Stabilized finite element formulations for incompressible flow computations. *Advances in applied mechanics* 1991; 28: 1–44.

39. Ganesan S, Srivastava S. ALE-SUPG finite element method for convection–diffusion problems in time-dependent domains: Conservative form. *Applied Mathematics and Computation* 2017; 303: 128–145.

40. Nobile F, Pozzoli M, Vergara C. Inexact accurate partitioned algorithms for fluid-structure interaction problems with finite elasticity in haemodynamics. *Journal of Computational Physics* 2014; 273: 598–617.

41. Crosetto P, Deparis S, Fourestey G, Quarteroni A. Parallel algorithms for fluid-structure interaction problems in haemodynamics. *SIAM Journal on Scientific Computing* 2011; 33(4): 1598–1622.

42. Bertagna L, Deparis S, Formaggia L, Forti D, Veneziani A. The LifeV library: engineering mathematics beyond the proof of concept. *arXiv:1710.06596* 2017.

43. Bonnemain J, I. Malossi AC, Lesinigo M, Deparis S, Quarteroni A, von Segesser LK. Numerical simulation of left ventricular assist device implantations: Comparing the ascending and the descending aorta cannulations. *Medical Engineering & Physics* 2013; 35(10): 1465-1475.

44. Guerciotti B, Vergara C, Ippolito S, Quarteroni A, Antona C, Scrofani R. A computational fluid-structure interaction analysis of coronary Y-grafts. *Medical Engineering & Physics* 2017; 47: 117-127.

45. Vergara C, Le Van D, Quadrio M, Formaggia L, Domanin M. Large eddy simulations of blood dynamics in abdominal aortic aneurysms. *Medical Engineering & Physics* 2017; 47: 38–46.

46. Fumagalli I, Fedele M, Vergara C, et al. An image-based computational hemodynamics study of the Systolic Anterior Motion of the mitral valve. *Computers in Biology and Medicine* 2020; 123: 103922.

47. Pozzi S, Domanin M, Forzenigo L, et al. A surrogate model for plaque modeling in carotids based on Robin conditions calibrated by cine MRI data. *Int. J. Numer. Methods Biomed. Eng.* 2021: e3447.

48. Bennati L, Vergara C, Domanin M, et al. A Computational Fluid-Structure Interaction Study for Carotids With Different Atherosclerotic Plaques. *Journal of Biomechanical Engineering* 2021; 143(9).

49. Gibson LJ. Biomechanics of cellular solids. *Journal of biomechanics* 2005; 38(3): 377–399.

50. Katritsis D, Kaiktsis L, Chaniotis A, Pantos J, Efstathopoulos EP, Marmarelis V. Wall shear stress: theoretical considerations and methods of measurement. *Progress in cardiovascular diseases* 2007; 49(5): 307–329.

51. Efstathopoulos EP, Patatoukas G, Pantos I, Benekos O, Katritsis D, Kelekis NL. Wall shear stress calculation in ascending aorta using phase contrast magnetic resonance imaging. Investigating effective ways to calculate it in clinical practice. *Physica Medica* 2008; 24(4): 175–181.

52. Khosravi A, Wendler O. TAVI 2018: from guidelines to practice. *European Journal of Cardiology Practice* 2018; 15: 29.

53. Elkayam U, Gardin J, Berkley R, Hughes C, Henry W. The use of Doppler flow velocity measurement to assess the hemodynamic response to vasodilators in patients with heart failure. *Circulation* 1983; 67(2): 377–383.

54. Johnson NP, Zelis JM, Tonino PA, et al. Pressure gradient vs. flow relationships to characterize the physiology of a severely stenotic aortic valve before and after transcatheter valve implantation. *European heart journal* 2018; 39(28): 2646–2655.

55. Quarteroni A, Veneziani A, Vergara C. Geometric multiscale modeling of the cardiovascular system, between theory and practice. *Computer Methods in Applied Mechanics and Engineering* 2016; 302: 193–252.